Evaluating the potential of SMART subsea cable pressure sensors to constrain Subpolar North Atlantic circulation variability through Observing System Simulation Experiments

Matthew Goldberg,[a] An T. Nguyen,[a] Helen Pillar,[a] , Bruce M. Howe,[c] Patrick Heimbach,[a,b]

[a] *Oden Institute for Computational Engineering and Sciences, The University of Texas at Austin, 201 E. 24th Street, C0200, Austin, TX 78712, United States of America*

[b] *Jackson School of Geosciences, University of Texas at Austin* [c] *University of Hawai'i at Manoa - JTF SMART Cables, 2525 Correa Rd. HIG 109B, Honolulu, HI 96822, United States of America*

Corresponding author: Matthew Goldberg, matthew.goldberg10@utexas.edu

ABSTRACT: Bolstering global ocean observing infrastructure is critical for understanding, quantifying, and predicting Earth's climate variability and change. While new observing technologies are in development, their deployment and calibration often span years before becoming fully operational. This study evaluates one such system: SMART (Science Monitoring And Reliable Telecommunications) Subsea Cables, which provide high-frequency, seafloor-based observations. We conduct Observing System Simulation Experiments (OSSEs) to quantify the potential of constraining the ocean circulation using simulated SMART sensor data. Within the Estimating the Circulation and Climate of the Ocean (ECCO) framework, we apply adjoint-based state and parameter estimation to constrain a Subpolar North Atlantic regional ocean model using synthetic ocean bottom pressure anomaly observations from a high-resolution global "nature run." Model skill is quantified using a score reflecting error reduction between the regional model trajectory and the nature run. Model gradients capture sensitivity information, revealing the significant role of atmospheric surface forcing uncertainty in bottom pressure variations. The forcing adjustments obtained through gradient-based optimization are validated for their dynamical relevance. Atmospheric pressure, followed by zonal and meridional surface winds, are identified as the primary control variables driving bottom pressure anomaly correction—consistent with physical oceanography theory. Assimilation of bottom pressure anomaly also improves estimates of barotropic (depth-integrated) transport and Arctic freshwater export, demonstrating the SMART system's potential to constrain basin-scale ocean circulation. These results underscore the value of high-frequency seafloor pressure data in reducing uncertainty in dynamically important ocean processes that lack constraint from sufficient observational infrastructure. SMART cables complement satellite altimetry and promise to enhance the spatiotemporal resolution of the global ocean observing system.

Significance Statement

The ocean plays a central role in regulating Earth's climate, but many important processes are poorly measured because existing observing systems do not adequately sample the global ocean. This study explores how commercial seafloor telecommunication cables equipped with scientific sensors could help fill those gaps. Using computer simulations, we show seafloor pressure measurements can reduce uncertainty in redistribution of water masses and freshwater due to ocean currents throughout the North Atlantic, a region critical for climate. We also find that changes in surface atmospheric pressure and winds strongly influence these signals. Moreover, high-frequency monitoring from seafloor cables effectively reduces uncertainty in sub-monthly ocean processes. These results suggest that sensor-equipped cables will be a powerful addition for quantifying circulation variability and improving climate predictions.

1. Introduction

The Science Monitoring And Reliable Telecommunications (SMART) subsea cable initiative represents a new frontier in ocean observation, enabling high-frequency seafloor monitoring through telecommunication infrastructure (Howe et al. 2019). As part of the United Nations Decade of Ocean Science for Sustainable Development, the Joint Task Force on SMART cable systems—established in 2012 by the International Telecommunication Union (ITU), the World Meteorological Organization (WMO), and the Intergovernmental Oceanographic Commission of UNESCO (UNESCO-IOC) and supported by more than 400 volunteer stakeholders—is working to enhance the Global Ocean Observing System (GOOS) by integrating scientific sensors into newly deployed subsea fiber optic cables. As one of four emerging GOOS networks complementing thirteen established ones, SMART cables will host instruments such as thermometers, seismic accelerometers, and pressure sensors, spaced approximately every 150 km. These sensor packages cannot be attached or augmented once the cable is in place, a design limitation driven by stringent regulations from the telecommunications industry that presents significant challenges in terms of the flexibility of future sensor upgrades or adjustments. Because of this restriction, it is critical to assess potential value in advance and best leverage opportunity for enhanced ocean constraint. Here, we use simulated data to quantify how *in situ* ocean bottom pressure (OBP) measurements can improve understanding of ocean dynamics and constraining ocean models.

OBP reflects the mass of the water column and varies in response to circulation change, tides, surface mass flux (e.g., precipitation, evaporation, runoff), and glacial melt. Currently, large-scale OBP is primarily observed from space via the Gravity Recovery and Climate Experiment (GRACE), which infers monthly-mean OBP anomalies p_b from changes in Earth's gravity field (Tapley et al. 2004, 2019). However, GRACE's spatial resolution of roughly 300 km limits its ability to resolve coastal dynamics and fine-scale topographic effects, particularly in regions of complex bathymetry. Furthermore, GRACE-based estimates suffer from significant temporal aliasing error, as their one-repeat-cycle monthly aggregate measurements are contaminated with the effects of high-frequency fluctuations in OBP (e.g., from tides, storm surges, barotropic motions, and eddies). While GRACE offers global coverage at coarse spatial and temporal resolution, SMART can potentially provide complementary *in situ* OBP observations with high temporal resolution.

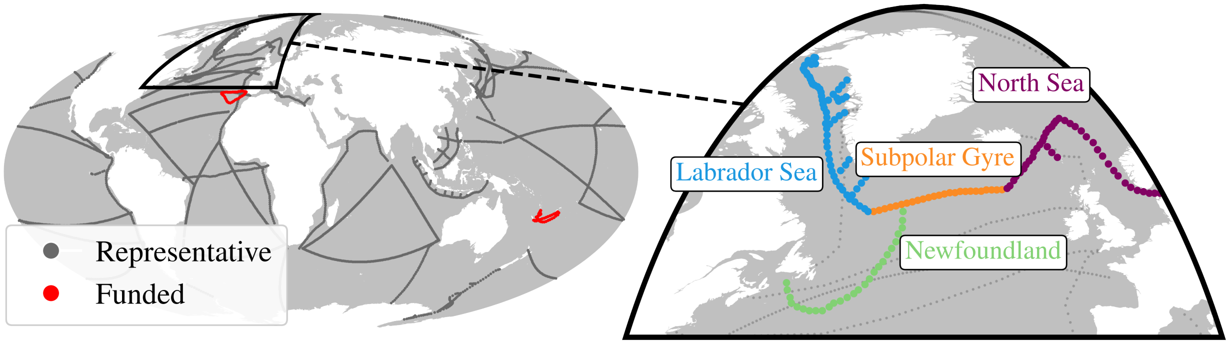

Fig. 1. (Left) Future global SMART cable network, including notional, proposed, and funded instruments. (Right) Subpolar North Atlantic cable and partial cables used in this study.

To quantify the potential benefit of SMART's addition for GOOS, we run observing system simulation experiments (OSSEs) using the Arctic Supolar gyre sTate Estimate (ASTE, Nguyen et al. 2021). Developed within the Estimating the Circulation and Climate of the Ocean (ECCO) consortium, ASTE employs adjoint-based data assimilation to constrain a coupled ocean-sea ice model to all available *in situ* and remotely sensed observations (Forget et al. 2015; Stammer et al. 2002; Nguyen et al. 2021). The adjoint model efficiently computes the sensitivity, or gradients, of model-data misfits to uncertain model parameters. Through nonlinear least-squares optimization, ASTE is iteratively brought into agreement with the data to within model and data errors. Importantly, ASTE's adjoint-based data assimilation is non-sequential, allowing model gradients to be computed over the state estimate's full integration time. As such, the resulting model-data synthesis represents a dynamically consistent time-evolving ocean-sea ice state that can be used for meaningful multi-decadal climate analysis and rigorous assessment of closed budgets at the grid-scale. In addition to informing a descent direction in an optimization landscape, as discussed further in Section 2a, adjoints find use in mechanistic studies as they illuminate dynamical ocean teleconnections (Heimbach et al. 2011; Pillar et al. 2016; Jones et al. 2018).

In this investigation, we focus on assessing the potential value of proposed SMART observations in the Suboplar North Atlantic (SPNA, Fig. 2). The SPNA is a critically important region for the Atlantic Meridional Overturning Circulation (AMOC). Variability in overturning here reflects a balance between horizontal wind-driven circulation and buoyancy forcing that drives vertical exchange and water-mass transformation, while boundary mixing further contributes to the formation of dense waters that supply the lower limb of the overturning circulation. This is also one of few areas where sustained observing systems already exist, such as the Overturning in the Subpolar North Atlantic Program (OSNAP) array (Lozier et al. 2017), long-term moorings (Handmann et al. 2018; Mercier et al. 2024; Curry et al. 2014) and tomographic arrays (Avsic et al. 2005) in the Labrador Sea and Davis Strait, providing observing systems against which SMART's value can be compared. The dynamic environment and topographic complexity of the SPNA make it an ideal proving ground for assessing the capacity of regional ocean models to assimilate high-frequency OBP data and improve estimates of key climate indicators such as overturning strength and volume transport through major gateways. Köhl et al. (2012) investigated the impact of assimilating monthly GRACE data into the German extension of ECCO's 1-degree global ocean state estimate, and showed that adjustments to the model's basin-scale OBP correlate with changes in the model's barotropic (depth-integrated) transport, except near the equator and along the coasts. This finding implies that even large-scale OBP corrections can influence the model's representation of integrated mass transport. However, while the low equatorial correlation is anticipated due to the breakdown of geostrophy, GRACE's coarse resolution and temporal smoothing are inadequate to properly characterize this correlation along coasts and other regions of highly variable topography. Moreover, Köhl et al. (2012) found that improvement in barotropic circulation representation was sensitive to the OBP product used with products differing regionally and close to land.

Building on Köhl et al. (2012)'s work, we investigate the OBP–barotropic transport relationship at daily timescales and finer spatial scales, leveraging the higher-resolution and more localized pressure constraints provided by proposed SMART cable paths. By resolving smaller-scale and higher-frequency (sub-monthly) variability in the SPNA, we aim to show SMART's observations can capture transport adjustments that may be obscured in coarser observing systems, thus offering new insights into the physical coupling between local pressure anomalies and regional circulation.

For established observing systems with readily available data, observing system experiments (OSEs) are commonly used to assess the system's impact. This is done by conducting twin experiments: one using the full observing system and another with one or more components withheld, referred to as observation denial experiments (e.g., Fujii et al. 2019). The impact of the withheld component is typically quantified by the difference in predefined model performance metrics between the two experiments. By design, these metrics can only be calculated where independent observations are available to serve as a reference, thus making the evaluation restricted to observed regions. This reliance on existing observations limits OSEs' applicability to proposed systems like SMART cables, for which independent validation data are unavailable in the relevant regions.

To assess the impact of future data, one can make use of OSSEs, which in contrast to OSEs use two models: a nature run (NR) and a forecast model (FM) (Hoffman and Atlas 2015; Zeng et al. 2020). A NR is a realistic model simulation that mimics the "true" system's state, e.g. the observed ocean. The NR is typically configured at very high resolution in order to capture phenomena occurring at scales smaller than the grid size of the FM. The steps involved in OSSEs include first sampling synthetic observational data from the NR and prescribing associated representation uncertainty based on the NR variance that is unresolved (i.e., sub grid-scale) in the FM. The synthetic observations are then assimilated into the FM. Finally, model diagnostics from the pre- and post-assimilation states are compared via a skill score, which quantifies the impact of the observing system in terms of how much closer the post-assimilation FM trajectory is to the analogous NR diagnostic.

Given the flexibility of this method and the existence of a high resolution ECCO 2-km global simulation (Gallmeier et al. 2013; Rocha et al. 2016; Wang et al. 2018; Arbic 2022) to serve as the NR as well as ASTE as the FM, we will employ OSSEs and assess the impact of SMART cables potential new OBP. The remainder of the paper is arranged as follows. Section 2 describes the OSSE design, including NR and FM configurations and specified synthetic data uncertainty. Section 3 presents results of OSSEs in the SPNA and a provides a discussion of model-data misfit reduction of p_b. Dynamical mechanisms underpinning propagation of assimilated p_b will also be discussed, as well as the subsequent constraint on barotropic velocities. Section 3d explores the constraint potential SMART OBP acquisitions exert on Arctic freshwater export. Finally, Section 3e compares the improvement seen by OSSEs involving synthetic SMART versus GRACE data. Section 4 provides a summary of the work and future outlook.

2. Methods

a. Data assimilation framework

The dynamical core of ASTE is the Massachusetts Institute of Technology general circulation model (MITgcm; Marshall et al. 1997; Adcroft et al. 2004). Nguyen et al. (2021) describes ASTE's optimization of its Release 1 solution (ASTEr1) in detail; we summarize the important points here. Initialized from a set of control variables $\mathbf{u}$, which are uncertain inputs required to integrate the model, the MITgcm evolves the ocean state $\mathbf{x}(t, \mathbf{u})$ in time through the hydrostatic primitive equations. Controls $\mathbf{u}$ include hydrographic initial conditions, surface atmospheric boundary conditions, and ocean mixing parameters such as isopycnal and diapycnal mixing. Given the many sources of model uncertainty, such as discretization approximations, initial conditions, and boundary conditions (see Wei et al. 2025), and additional uncertainty in the observations, data assimilation amounts to an inverse problem in which the uncertain model controls $\mathbf{u}$ are adjusted such as to minimize the model-data misfit and produce a solution consistent with observations within this uncertainty. The adjoint method enables computation of the gradient of a given model scalar diagnostic (i.e. the misfit cost function, below) to *all* model controls. In the ECCO framework, algorithmic differentiation using the Transformations in Fortran (TAF) library produces the ocean model's derivative code, enabling computation of adjoint sensitivities (Giering and Kaminski 1998).

In a least-squares optimization, a misfit cost function J describes the gap between N observational data $\mathbf{y} = [y_1, \ldots, y_N]^T \in \mathbb{R}^N$ and model equivalents (or simulated observations) obtained via the parameter-to-observable map $\hat{\mathbf{y}} = \mathbf{Obs}(\mathbf{x}(\mathbf{u})) = [\mathbf{Obs}_1(\mathbf{x}(\mathbf{u})), \ldots, \mathbf{Obs}_N(\mathbf{x}(\mathbf{u}))]^T \in \mathbb{R}^N$:

$$J(\mathbf{u}) = \underbrace{\frac{1}{2}(\mathbf{y}-\hat{\mathbf{y}})^{\mathrm{T}}\mathbf{\Gamma}_{\mathrm{obs}}^{-1}(\mathbf{y}-\hat{\mathbf{y}})}_{J_{\mathrm{misfit}}(\mathbf{u})} + \underbrace{\frac{1}{2}(\mathbf{u}(0)-\mathbf{u}_0)^{\mathrm{T}}\mathbf{\Gamma}_0^{-1}(\mathbf{u}(0)-\mathbf{u}_0)}_{J_0(\mathbf{u})} + \underbrace{\frac{1}{2}(\mathbf{u}-\mathbf{u}_{\mathrm{BC}})^{\mathrm{T}}\mathbf{\Gamma}_{\mathrm{BC}}^{-1}(\mathbf{u}-\mathbf{u}_{\mathrm{BC}})}_{J_{\mathrm{BC}}(\mathbf{u})}. \tag{1}$$

The second term encodes our *a priori* knowledge about the initial condition controls $\mathbf{u}_0$, penalizing deviations from first-guess controls based on the control uncertainty operator $\mathbf{\Gamma}_0$. The third term is similar to the second, but is meant to distinguish initial from boundary condition controls $\mathbf{u}_{\mathrm{BC}}$. In practice, the structure of $\mathbf{\Gamma}_0$ and $\mathbf{\Gamma}_{\mathrm{BC}}$ are poorly known. The diagonal elements, which represent the uncertainty associated with each first-guess control at each grid cell in the domain, can be estimated with effort. The off-diagonal elements, which describe how uncertainties at different locations within a control field are related, are much more difficult to determine (Wunsch and Heimbach 2007). A similar limitation applies to the observational uncertainty operator $\mathbf{\Gamma}_{\mathrm{obs}}$ discussed further in Section d. As noted by Wunsch and Heimbach, full error covariance matrices in oceanography are rarely estimated. Most ECCO-based optimization applications assume $\mathbf{\Gamma}_{\mathrm{obs}}$, $\mathbf{\Gamma}_0$, and $\mathbf{\Gamma}_{\mathrm{BC}}$ to be diagonal. This effectively treats uncertainties at different locations as uncorrelated. In some cases, spatial smoothing constraints are applied as a substitute for explicit off-diagonal structure, thereby introducing an implicit form of correlation. Even so, the diagonal terms themselves often rely on subjective judgment and interpretation of the broader oceanographic literature.

The gradients obtained by the adjoint method solve $\mathbf{u}_{\min} = \min_{\mathbf{u}} J$ via gradient descent. Repeated iterations perturb controls in a way that steers the model trajectory towards observations. Following Loose et al. (2020), we assess the relative importance of each control in the optimization as follows:

$$||u||^2 = \sigma_J^{-2} \sum_{i,j} \left(\frac{\partial J}{\partial u(i,j)} \sigma_u(i,j) \right)^2 \in [0,1]. \tag{2}$$

The sum of control contributions across all controls is identically 1. Above, $\sigma_u(i,j)$ comprises the diagonal entries of $\mathbf{\Gamma}_0$ or $\mathbf{\Gamma}_{\mathrm{BC}}$ and the cost function variance (e.g. for BC controls) $\sigma_J = \sqrt{[\nabla_{\mathbf{u}} J]^T \mathbf{\Gamma}_{\mathrm{BC}} \nabla_{\mathbf{u}} J}$ normalizes the weighted sensitivities. This normalization is necessary to prevent controls with differing magnitudes and prior uncertainties from dominating analysis due to scale alone.

b. OSSE forecast model (FM)

A modification of ASTEr1 is the designated FM for the OSSEs in this study. The ASTE domain covers the Atlantic northward of 32°S, as well as the Arctic and neighboring seas. The state estimate captures accurate transports of volume, heat, and freshwater in the North Atlantic and Arctic, having been constrained to $\mathcal{O}(10^9)$ data, including from satellite, autonomous profiler, and moorings. Gridded in a latitude-longitude-polar cap (LLC) configuration, its horizontal resolution is configured at $1/3°$, or about 22 km in the SPNA, with 50 vertical levels ranging from 10 m at the surface to 450 m at the ocean bottom. It is forced by lateral boundary conditions obtained from the ECCO Version 4 Release 3 (ECCOv4r3, Fukumori et al. 2017) solution and first-guess atmospheric forcing fields from the Japanese 55-year Reanalysis (JRA-55; Kobayashi et al. 2015) that have been modified as a result of the gradient-based optimization. The state estimate spans the period 2002-2017 and provides an acceptable fit to observational data. While ASTEr1 applies a constant atmospheric pressure (p_{atm}) loading of about 10^5 Pa everywhere and excludes it from the set of optimization controls, we instead apply and optimize JRA-55 atmospheric pressure, which is known to drive p_b changes on intra-seasonal timescales (Stepanov and Hughes 2006; Na et al. 2016). Both ASTEr1 and the modified version use a no-slip bottom boundary condition with quadratic bottom drag, as well as a nonlinear free surface (Adcroft et al. 2004) and real freshwater forcing (Campin et al. 2004).

Fig. 2 shows the first proposed system of SMART cables within the SPNA, whose positions spans 73E to 9W and connects Baffin Bay to the North Sea, with a branch emanating from the Eastern Labrador Sea southward towards Northeastern Canada. This presently planned cable system cuts through key high-latitude gateways such as the Davis Strait and the Iceland-Faroe channel, and can potentially provide measurements relevant to monitoring elements of the AMOC.

c. OSSE nature run (NR)

An existing free-running non-assimilated MITgcm simulation configured on the LLC grid at $1/48°$ horizontal resolution generally referred to in the literature as the MITgcm LLC4320 run (e.g., Gallmeier et al. 2013; Rocha et al. 2016; Wang et al. 2018; Arbic 2022), serves as the NR for this study. This solution provides hourly diagnostics for the 14 months between September 2011 and November 2012. The NR differs from the FM primarily in its eddy-resolving resolution,

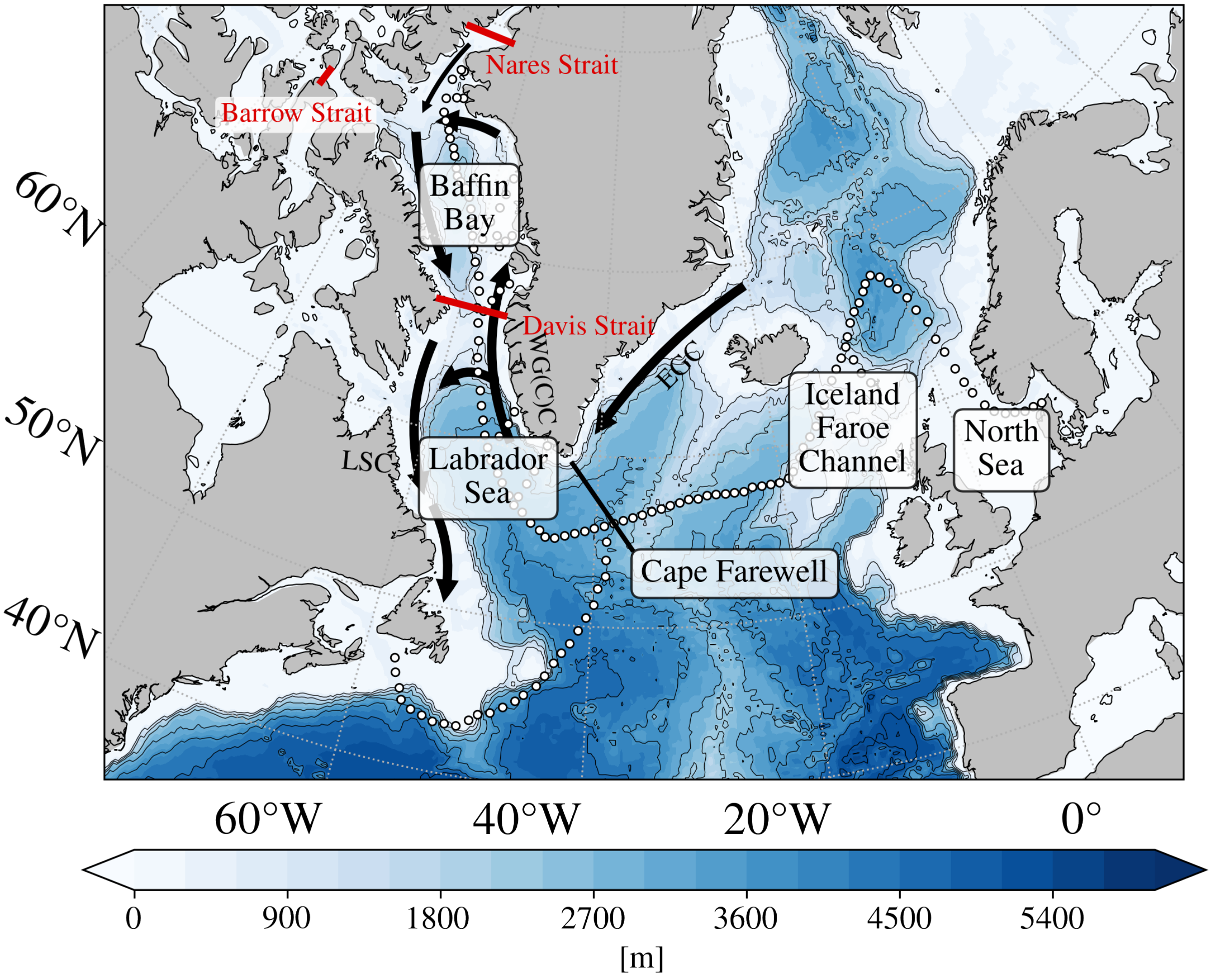

Fig. 2. The SPNA region with Seas, straits (red lines), and oceanographic currents (black arrows) discussed in this study labeled. Color map and contours show bathymetry in ASTE. EGC, WG(C)C, and LSC abbreviate East Greenland Current, Western Greenland (Coastal) Current, and Labrador Sea Current, respectively. The sensor locations along the Subpolar North Atlantic cable system, spaced approximately 70 km apart, are shown with white dots and are points at which synthetic observations will be extracted from the nature run.

approximately 2 km in the SPNA, and additional physics such as tidal forcing (Arbic 2022). The LLC4320's submesoscale structures have been validated against satellite data (Gallmeier et al. 2013). Table 1 compares the FM and NR configurations.

The NR provides model diagnostic variables from which we extract synthetic SMART cable observations. A set of hypothetical sensors defined by their (ungridded) lat-lon coordinates (Fig. 2) constitutes a cable. Sensors are spaced roughly 70 km apart, falling within the planned spacing

	forecast model (ASTE)	nature run (LLC4320)
Domain	Regional (Atlantic + Arctic + North Pacific)	Global
Horizontal grid spacing at equator [degrees]	1/3	1/48
Vertical levels	50	90
Surface level thickness [meters]	5	1
Atmospheric forcing	3-hourly JRA-55 bulk formulae (Kobayashi et al. 2015) + optimized control adjustments	6-hourly ERA-interim analysis 0.14-degree grid bulk formulae
Atmospheric load	Yes	Yes
Tides	No	Yes
Barotropic time-stepping	Adams-Bashforth	Crank-Nicolson
Time step [seconds]	1200	25

TABLE 1. Comparison of FM to NR.

estimated between 60 and 150 km (Howe et al. 2019). A nearest-neighbor search maps sensor locations to their analogous model grid points, accounting for the irregular LLC grid curvature. Given the NR's higher resolution, a horizontal, area-weighted binned average allows for direct comparison of FM and NR bottom pressure sensors's data.

d. Synthetic data processing and uncertainty

Spatial and temporal resolution differences between NR and FM motivate the data processing steps described in this section. Raw OBP data from the NR's native grid at hourly frequency were processed temporally at each grid point as follows. First, a time-mean over the NR's 14 month duration was removed from each raw OBP data point to eliminate the dynamically unimportant systematic offset arising from differences in local bathymetry between NR and FM. The data were then stripped of a linear trend before being detided of the sixteen leading tidal constituents, as tides are absent from the FM. Next, domain-wide monthly means were computed and removed to eliminate the seasonal cycle. Finally, these OBP anomalies were binned temporally to produce daily observations p_b . The resultant p_b signals were then spatially bin-averaged to coarsen the NR p_b data to match the FM's horizontal resolution (see Table 1).

The above-described procedure yields an FM-equivalent synthetic p_b data set for use to constrain the FM. In addition to the synthetic data, an associated data uncertainty ($\mathbf{\Gamma}_{\text{obs}}$ in Eqn. 1) is also required prior to performing the OSSE. This $\mathbf{\Gamma}_{\text{obs}}$ can be thought of as containing both instrumental errors (applicable for real observations) and the FM's model representation error, i.e., the extent to which the FM's horizontal grid cannot adequately render observed, or in this case the NR's physical processes (see e.g., Nguyen et al., 2020). To estimate the time-invariant two-dimensional representation error, we compute the combined space-time standard deviations of the detided/detrended/de-seasonalized NR's daily p_b over each of the equivalent FM's grid-size box. As an example, at a given FM's grid location, we identify all NR's 16×16 grid boxes' p_b daily anomalies spanning the entire 14-month record and compute the square-root of the variance of these p_b anomalies. In the last step, we convert the synthetic p_b data and uncertainty $\mathbf{\Gamma}_{\text{obs}}^{1/2}$ to equivalent water thickness through multiplication of the scalar constant $1/(g\rho_0)$, where ρ_0 is the constant density 1029 kg m^{-3} and g is the gravitational constant 9.81 m s^{-2}. The derived $\mathbf{\Gamma}_{\text{obs}}^{1/2}$ field (Fig. 3) shows high values along the coastal regions, an expected result due to shallow bathymetry and heightened influence of physical processes affecting p_b. Similarly, the high velocities and eddy activity in the Gulf Stream give rise to larger transport variability, and in turn higher p_b variability within each 16×16 patch. From the perspective of uncertainty, due to its lower resolution, the FM cannot be expected to capture the high variability simulated by the NR in these regions. Thus the corresponding high uncertainty here allows the FM to capture the NR's derived synthetic p_b to only within this error to be considered successful (Nguyen et al. 2020).

We summarize $\mathbf{\Gamma}_{\text{obs}}$ as the combination of the representation and the instrument errors,

$$\mathbf{\Gamma}_{\text{obs}} = (\text{Std}\,(p_b) + \mathbf{\Gamma}_{\text{instr}})^2,$$

where p_b represents the NR's detided, detrended, and space-time binned synthetic OBP daily anomaly. Normally distributed values with a 10 Pa (1 mm equivalent water height) standard deviation comprise $\mathbf{\Gamma}_{\text{instr}}$, following SMART cable's OBP accuracy requirement (JTF Engineering Team 2016). Clearly, the representation uncertainty in Fig. 3 eclipses the instrument error in magnitude. Finally, for simplicity it is assumed that uncertainties are independent across observations, i.e. that $\mathbf{\Gamma}_{\text{obs}}$ is diagonal.

We target reduction of the time-dependent p_b misfit costfunction.

$$J_{\text{misfit}}(\mathbf{s}) = \frac{1}{2}\mathbf{s}^T\,\Gamma_{\text{obs}}^{-1}\,\mathbf{s}, \tag{3}$$

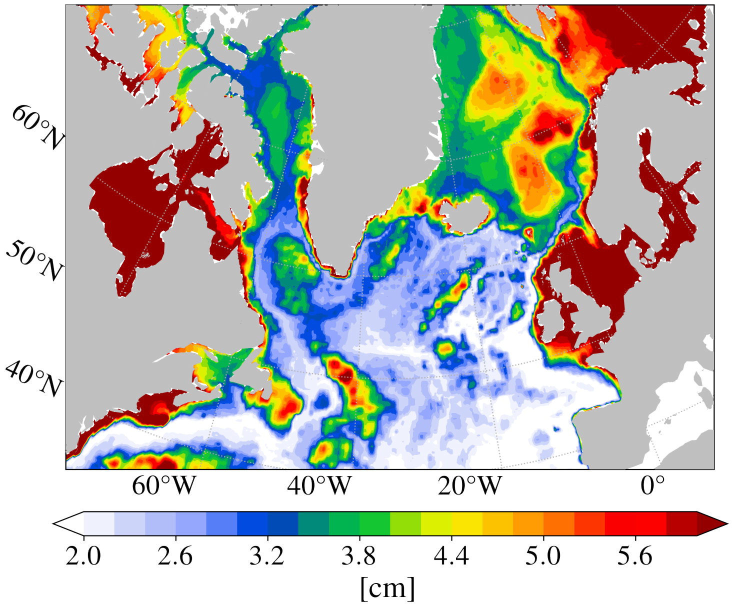

FIG. 3. Derived $\mathbf{\Gamma}_{\text{obs}}^{1/2}$ in equivalent cm of water height. This field, derived from taking the space-time standard deviations of the synthetic daily p_b anomalies, captures the error inherent in NR-FM comparison during data assimilation.

where

$$\mathbf{s} = \mathbf{S}\left[(\mathbf{y} - \overline{\mathbf{y}}) - \left(\hat{\mathbf{y}} - \overline{\hat{\mathbf{y}}}\right)\right].$$

with $\overline{\bullet}$ implying the time mean over the length of the assimilation experiment, following Fukumori et al. (2017). Assimilating model anomalies to data anomalies essentially allows the cost function to target *variability* rather than mean behavior. We do, however, find a systematic shift in OBP accompanies adjustment of the anomaly. We quantify this shift as

$$\delta\text{OBP} = \overline{\widetilde{\text{OBP}} - \text{OBP}}, \tag{4}$$

where again $\tilde{\bullet}$ distinguishes the solution or post-assimilation OBP field and $\bar{\bullet}$ indicates the time-mean over the OSSE duration.

S is an isotropic spatial smoother function, which filters out bottom pressure misfit anomaly signals below 300 km. This smoothing focuses on reducing large-scale biases and improving the representation of oceanic and atmospheric processes at these scales, rather than addressing potential noisy grid-scale variations (Forget et al. 2015). In the results ahead, it is prudent to examine the spatial distribution of model-data discrepancies, i.e. the spatial fields that, when squared and summed in space and time, yield J_{misfit}. To this end, we coin the "spatial misfit" at fixed time t to be the field given by $\mathbf{s}(\mathbf{x}(t))/\sigma_{\text{obs}}^{1/2}$ where σ_{obs} are the (diagonal) elements of $\mathbf{\Gamma}_{\text{obs}}$.

e. Iterative optimization

Fig. 4 provides a high-level summary of an OSSE. The unconstrained FM runs for a predetermined simulation time, producing model diagnostics ϑ. We call this unconstrained run the "reference" experiment. Next, an identical FM run is performed, this time with the assimilation of a set of synthetic observations sampled from the NR. After several iterations, adjustments made to the control space reduce the discrepancy between model and synthetic data below some tolerance. A final FM run is performed with the optimized controls. We call this final run the "solution" or constrained experiment, and denote its model diagnostics as $\tilde{\vartheta}$. Finally, a skill score $\mathcal{S}$ measures the improvement in the constrained experiment as its proximity to the NR relative to the unconstrained experiment via the root-mean-square error (RMSE) as follows,

$$\mathcal{S} = 1 - \frac{\text{RMSE}(\tilde{\vartheta}, \vartheta^{\text{NR}})}{\text{RMSE}(\vartheta, \vartheta^{\text{NR}})}, \tag{5}$$

where ϑ^{NR} is the analogous diagnostic field from the NR. In the case of a 2D temporally varying field ϑ, the RMSE can be computed along the time axis at each spatial point. In the ensuing 2D skill map, a positive (negative) skill score indicates a more (less) accurate solution than reference forecast. For example, a skill of 0.1 indicates a modest but positive improvement in the FM's representation of ϑ's variability, reflecting a 10% reduction in RMSE relative to the pre-assimilation state. Note that skill is similar to the model-data misfit in that it quantifies the difference between FM and NR, but importantly it does so relative to the reference state of the field under consideration. Equivalently, positive skill can be understood as an increase in explained variance (see Appendix A1).

In the first OSSE in this study, we run the FM for the month of January, 2012, assimilating synthetic daily p_b data at each sensor in the SPNA cable. The month-long duration is motivated by the goal of providing analysis of daily variability complementing Köhl et al. (2012). The control vector $\mathbf{u}$ contains the following 8 atmospheric input variables: air temperature T_{air}, precipitation

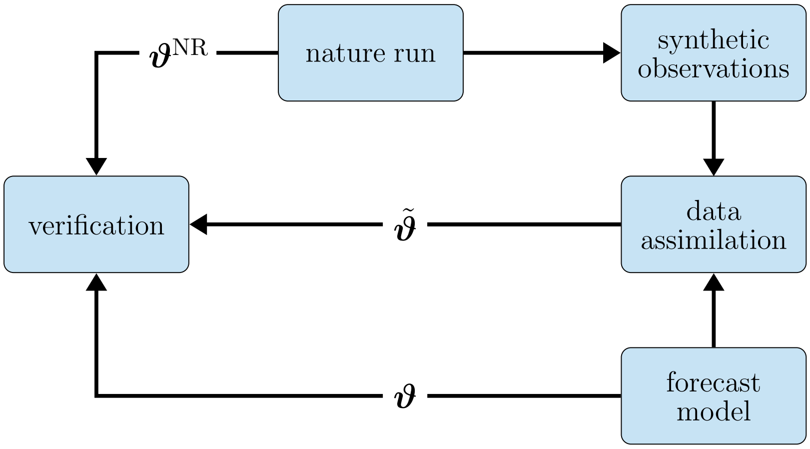

FIG. 4. OSSE flowchart adapted from Hoffman and Atlas (2015). Synthetic observations from the NR are assimilated into the FM. Solution and reference experiment fields $\tilde{\vartheta}$ and ϑ, respectively, are verified against the analogous NR output ϑ^{NR} using a skill score (Equation 5).

P, downward shortwave radiation R_{sw} and longwave radiation R_{lw}, specific humidity q_{air}, zonal wind u_w, meridional wind v_w, and atmospheric pressure p_{atm}. To test the sensitivity of p_b misfit reduction to control frequencies, we will perform OSSEs using daily (Section 3 and biweekly control adjustments (not shown). All but atmospheric pressure are initialized from ASTEr1 optimized adjustments and interpolated to daily from their original biweekly frequency. Control uncertainties $\sigma_{\mathbf{u}}$ are identical to those used in ASTEr1, except for atmospheric pressure which is obtained from the standard deviation of daily-mean values from JRA-55 for the year 2012. We note that there are other approaches to estimate this field, and derived an alternative in Appendix B1 following Chaudhuri et al. (2014). We will show later in Section 3b that our results are robust and not dependent on how this uncertainty field for p_{atm} is derived. The control adjustment frequency is discussed further in Section 3b. Given its novelty to ASTE, we impose no penalty on deviations from the atmospheric pressure control in the regularization term ($\mathbf{\Gamma}_{\mathrm{BC}}^{-1}$ for p_{atm} is set to zero in J_{BC} in Equation 1) in our OSSEs.

3. Results

a. SPNA cable OSSE

Fig. 5a shows the spatial p_b misfit on January 1, 2012 after one iteration of optimization, at which point the cost has been reduced by about 9%. Spatial misfit plots on subsequent days are

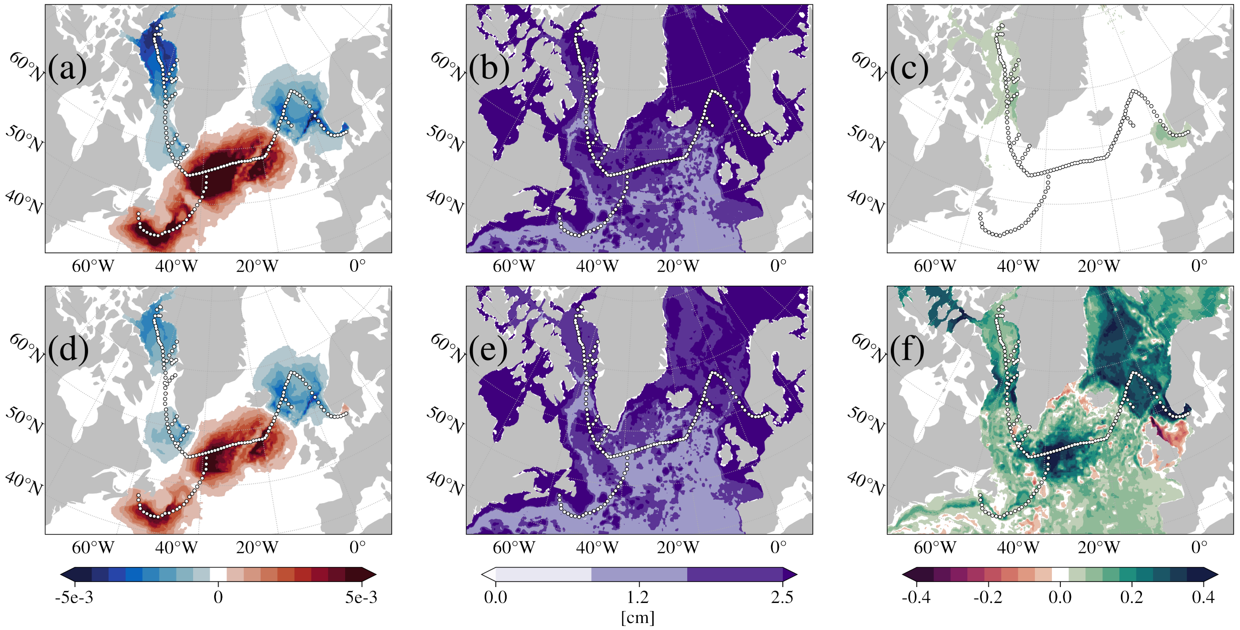

FIG. 5. (a) Normalized SPNA cable p_b spatial misfit on January 1, 2012 after one optimization iteration. Neighboring sensor misfits are smoothed, resulting in large positive and negative signals surrounding the cable. (b) Root mean-squared error RMSE($\tilde{p}_b, p_b^{\mathrm{NR}}$) measuring how far FM p_b is from NR p_b after assimilating synthetic cable observations from the NR. The RMSE field is compared to the corresponding "before-assimilation" RMSE(p_b, p_b^{NR}) (not shown), yielding, following Equation 5, skill $\mathcal{S}$ (c). Positive (negative) skill indicates regions in which the FM's p_b representation grew closer to (further from) that of the NR. (d-f) are the same as (a-c) but after 20 optimization iterations. Here, we show only the high-latitude region of ASTE occupied by the proposed SMART cable, where misfit reductions are largest.

qualitatively comparable, with positive and negative signals surrounding the cable. The RMSE at this iteration is shown in Fig. 5b. Owing to shallow bathymetry and in turn high p_b variability, the FM and NR have differing p_b representation in the North Sea and the region of Atlantic Canada in the vicinity of (65°W, 45°N), and in turn high RMSE. This RMSE is compared to the pre-assimilation RMSE (not shown), yielding, following Equation 5, the skill score $\mathcal{S}$ as shown in Fig. 5c. While the state of January p_b is largely similar to the pre-assimilation state, the green contours in Baffin Bay and the North Sea indicate regions that saw a p_b error reduction of roughly 5%. After 20 optimization iterations and a cost reduction of 86%, spatial misfit (Fig. 5d) and RMSE (Fig. 5e) reduction, and in turn p_b skill increase (Fig. 5f) can be seen not only along almost the entirety of the cable, but also throughout the wider SPNA region and into the Greenland, Iceland,

and Norwegian Seas. The reduction achieved is in part dependent on the user-provided steepest descent step length, which we fix at 5%. Comparing Fig. 5c and Fig. 5f, regions such as Baffin Bay and the northern North Sea continue to exhibit large positive skill. In the southern North Sea, a negative skill region emerges. In order to understand this regional dependency, we investigate the physics underlying adjustments obtained during assimilation.

b. Atmospheric control adjustments

The scalar misfit J_{misfit} (Equation 3) captures an aggregate of model-data p_b discrepancies across all sensors and all observation times. As such, it can be difficult to anticipate which sensors experience the greatest misfit reduction, and which locations see the highest skill in p_b. To disentangle contributions the SPNA cable's limbs exhibit during assimilation, subsequent OSSEs partition the SPNA cable into four branches (see Fig. 1 inset), dubbed the Labrador Sea, Newfoundland, Subpolar Gyre, and North Sea "partial cables". An ensemble of one-month OSSEs is performed for each partial cable for the months of January, April, July, and October of 2012, assimilating daily p_b misfits as in the full SPNA OSSE discussed in the previous section.

In every OSSE in the ensemble, p_{atm} dominates the optimization control adjustments, contributing to 98% of the misfit reduction relative to the other controls' adjustments using Equation 2. However, because no penalty restricts atmospheric pressure adjustments, there is a risk that the optimization will employ unreasonably large, unphysical adjustments to force misfit reduction. As such, atmospheric pressure adjustment magnitudes must be validated against typical range of p_{atm} in available reanalysis. Fig. 6 (top) shows the average standard deviation of daily atmospheric pressure from JRA-55 for the year 2012, where the average is computed across daily-binned records. The squares of this field populates the diagonal elements in the block of the covariance matrix $\mathbf{\Gamma}_{\text{BC}}$ pertaining to p_{atm}. In Fig. 6 (bottom), time series of daily JRA-55 atmospheric pressure standard deviation are shown in black with gray error envelopes computed from the standard deviation across 3-hourly records within each day. Such time series are plotted for the four months and four partial cables for which OSSEs were conducted. The colored time series show each OSSE's average absolute value of atmospheric pressure adjustments after 20 iterations of optimization for each day of the OSSE. Both forcing and adjustment time series are computed as the mean across all sensors in a given cable. Note that JRA-55 data resides on a different grid than ASTE, so their

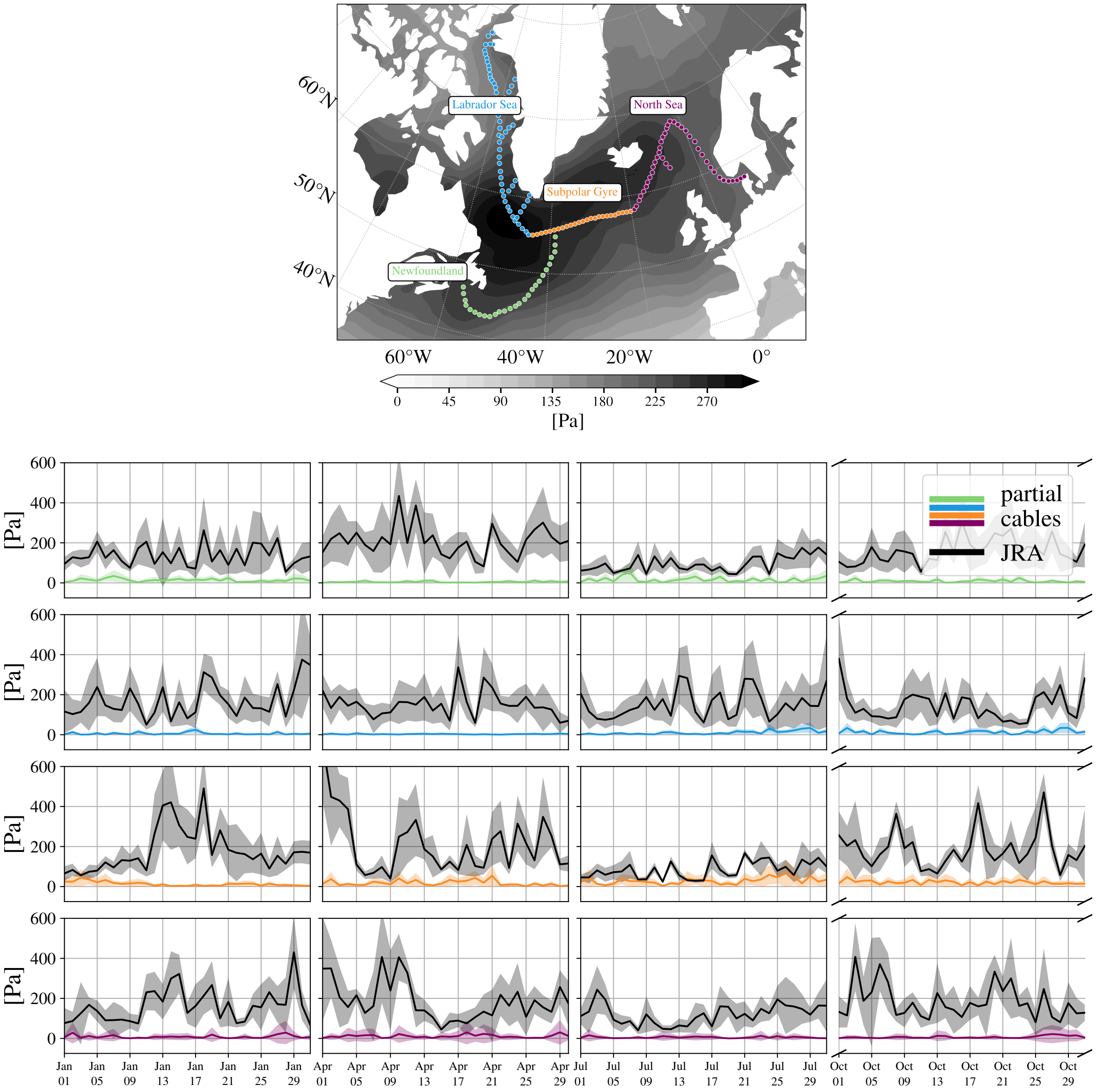

Fig. 6. (Top) Standard deviation of daily binned 2012 JRA-55 surface pressure, averaged over the year, with the locations of the 4 cable segments used in the "partial cable" OSSEs shown in color. Values are on the order of 10^2 Pa and are used as prior uncertainty for the p_{atm} control. (Bottom) Colored curves show mean absolute value of p_{atm} adjustments for four partial cable OSSEs (rows) for each of the four months of 2012 (columns) used in the OSSE ensemble, with shaded envelopes denoting standard deviations. Black curves show daily JRA-55 standard deviations, with grey envelopes indicating sub-daily variability. Each point in every time series is computed as an average across sensors in a given partial cable. p_{atm} adjustments remain well below JRA-55 variability, confirming that assimilation does not introduce unphysical corrections.

time series' values are computed at the sensor locations using a nearest neighbor interpolation. In general, the control adjustment variability magnitudes are much smaller than that of the forcing field, indicating that the corrections made during optimization are sensible. In other words, no extreme atmospheric pressure adjustments are made to overfit the model to the observations. We note further in Appendix B1 that our sensible p_{atm} adjustments are robust independent of the choice of p_{atm} uncertainty used.

Fig. 7 shows spatial misfit and control adjustments from the January OSSE for the Subpolar Gyre cable for iterations 1 and 20. During the optimization, a prominent dipole in p_b misfit in the SPNA is offset by adjustment of p_{atm}, which acts to increase (reduce) loading over the regions of negative (positive) misfit. The p_{atm} adjustments are spatially diffuse relative to the spatial misfit, due both to smoothing (Section 2d) and oceanic teleconnections propagating the influence of assimilated p_b away from the cable over the OSSE duration. Note that the same mechanism drives the full SPNA cable OSSE, but p_{atm} adjustments throughout the region interfere with one another and are less interpretable. As atmospheric pressure increases (decreases), the water column shrinks (grows),

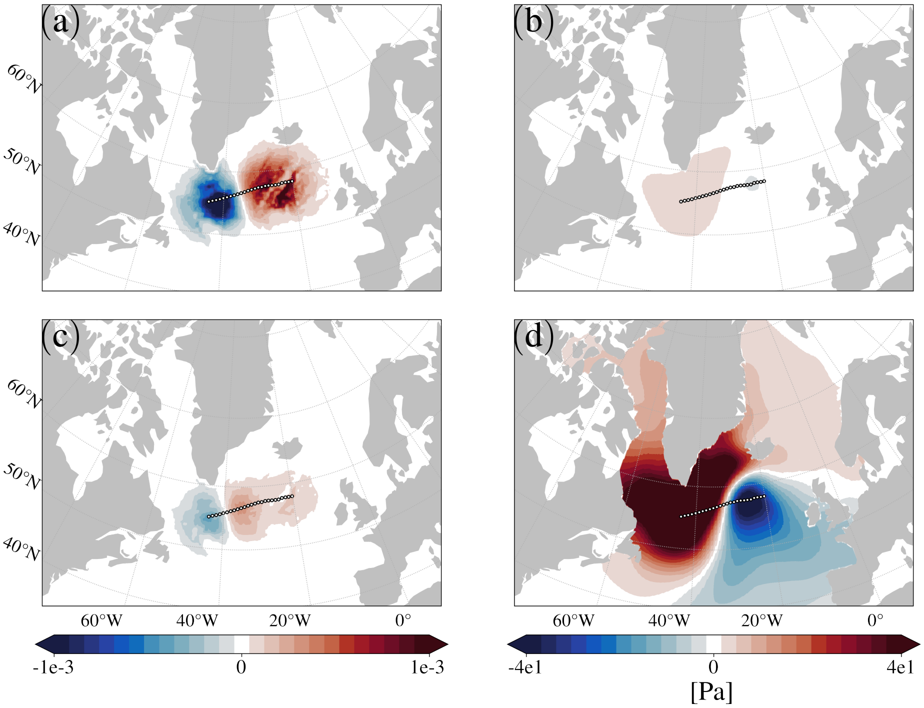

FIG. 7. (a) A smoothed and normalized p_b spatial misfit along the Subpolar Gyre cable appears as a negative-positive dipole. (b) A small positive (negative) adjustment to atmospheric pressure p_{atm} attempts to reduce the negative (positive) spatial misfit signal in the first optimization iteration. (c) and (d) show the same fields after 20 optimization iterations, at which point the spatial misfit has decreased due to the applied p_{atm} adjustment. The adjustment now exhibits a clear positive-negative dipole, the opposite of the spatial misfit pattern.

thereby increasing (decreasing) p_b. The next largest contributors are zonal and meridional surface winds adjustments. Changes in wind stress induce an Ekman transport response. In the Northern Hemisphere, positive (negative) wind stress curl induces Ekman convergence (divergence), raising (lowering) sea surface height and in turn bottom pressure anomaly. This mechanism is known to drive changes in seasonal bottom pressure anomaly (Chen et al. 2023). To see this mechanism more clearly in our study, we repeat the OSSEs without the atmospheric pressure control in order to isolate the effect due to surface winds. Similar skill (not shown) confirms the mechanism with associated wind stress curl adjustments driving bottom pressure anomaly misfit reduction. Section 3d further examines this mechanism.

Both the ASTEr1 and ECCO global solutions used biweekly atmospheric control adjustments. We found daily control adjustments to be critical to attain largely positive skill scores in this study.

When using biweekly control adjustments (not shown), while the cost reduces, in many cases the p_b skill patterns exhibit large negative swaths, which is likely a temporal aliasing consequence, as biweekly control adjustments cannot properly reduce daily misfits associated with our high frequency daily synthetic data. This highlights the importance of formulating the state estimate to fully leverage available observational constraints (i.e., by having high frequency adjustments to capture the high frequency variability observed in data).

c. Barotropic velocity

OBP fluctuations on sub-monthly timescales are known to be primarily barotropic (Bingham and Hughes 2008). Therefore, daily OBP data should impose a constraint on zonal and meridional components of depth-integrated velocity. This relationship has been investigated on seasonal timescales by Köhl et al. (2012), in which perturbations to p_b are shown to correlate with perturbations to barotropic streamfunction anomaly during monthly GRACE data assimilation. We extend Köhl et al. (2012) findings to obtain the barotropic velocity response through assimilating daily SMART observations. The barotropic velocity skills, obtained again by applying Equation 5 and using the NR and FM model diagnostics of daily depth-integrated zonal and meridional velocity components. Fig. 8 shows the meridional barotropic velocity V_{bt} skills obtained after only one optimization iteration. The corresponding zonal components (U_{bt}, not shown) take on skill of similar magnitude and sign to V_{bt}. As hypothesized, these velocity skill patterns (Fig. 8e-h) from the partial-cable experiment closely resemble their p_b counterparts in (Fig. 8a-d). In addition to agreeing with the theoretical relationship between water-column mass and depth-integrated velocity, the results shown in Fig. 8 emphasize the utility of SMART's high-frequency observations: ocean quantities can be measured *indirectly* from SMART sensing.

The spatial scale over which adjustments occur is set predominantly by the distance fast barotropic waves can propagate to reach the array over the model integration period of one month, as seen in the regions surrounding the Subpolar Gyre cable in the control adjustments in Fig. 7. These adjustments reduce the misfit along and nearby the cable, leading to the diffuse skill patterns seen in Fig. 8. Furthermore, the full SPNA cable skill pattern (Fig. 5f) resembles a superposition of the component experiments in Fig. 8 (a-d). High-skill regions that dominated the partial cable experiments, such as Baffin Bay in the Labrador Sea cable experiment, the heart of the Subpolar

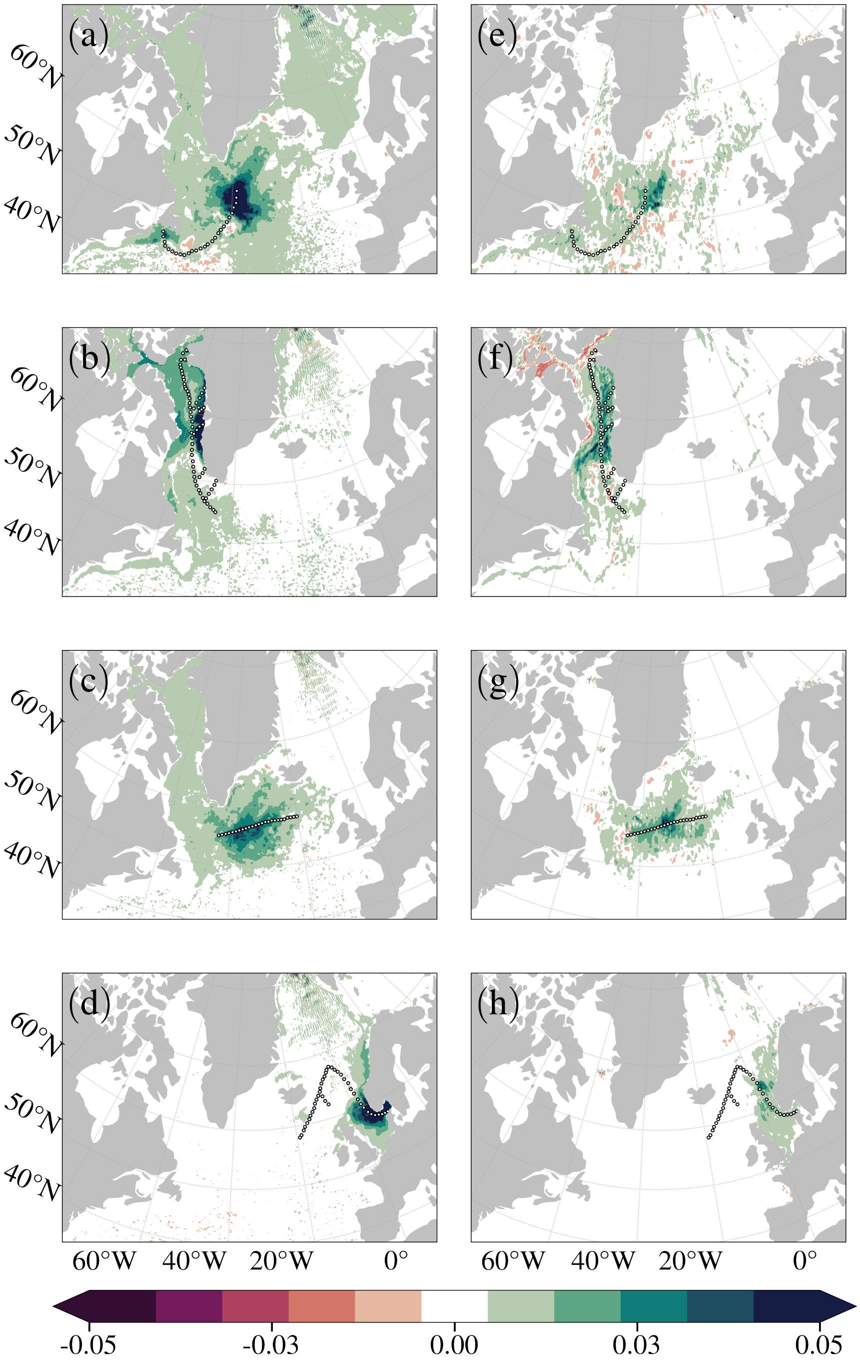

FIG. 8. p_b (a-d) and meridional barotropic velocity (e-h) skill scores after one optimization iteration for the four January 2012 daily-control partial cable experiments. The zonal skill scores (not shown) resemble their meridional counterparts. Similar patterns are obtained for the months of April, July, and October (not shown).

Gyre in the Subpolar Gyre cable experiment, and the North Sea in the North Sea cable experiment, still do so in the combined SPNA cable OSSE. Negative skill spots are visible in the U_{bt} and V_{bt} fields, and are primarily due to high-resolution NR velocity features that the FM is, by design, unable to resolve.

OBP, U_{bt}, and V_{bt} are shown to be sensitive to the same atmospheric forcings and subject to the same resulting oceanic adjustments. These shared dynamical underpinnings create potential value for SMART to robustly constrain SPNA circulation upon assimilation (Loose et al. 2020; Loose and Heimbach 2021). The results presented above motivate us to examine the constraint SMART OBP may exert on other remote climate-relevant quantities of interest, such as freshwater exports from the Arctic, which are poorly constrained but estimated to be undergoing notable changes, with potentially significant downstream impacts on the AMOC (Haine 2020).

d. Advective freshwater flux anomaly

We focus on two major routes through which Arctic freshwater (FW) reaches the SPNA via two primary routes (Jahn et al. 2010; Haine et al. 2015). The first pathway is through Fram Strait, where FW is transported southward by the East Greenland Current (EGC, Fig. 2). As the current rounds Cape Farewell, it bifurcates: one branch, the Western Greenland Current (WGC), continues westward into the Labrador Sea joining the Labrador Sea Current (LSC), while the other, the Western Greenland Coastal Current (WGCC) turns northward through Davis Strait into Baffin Bay (Pacini and Pickart 2022). A secondary route delivers Arctic FW through narrow passages in the Canadian Arctic Archipelago including the Nares and Barrow Straits. Along this path, sea ice travels southward along the western coast of Baffin Bay and exits through Davis Strait, joining the Labrador Sea Current (LSC) (Münchow and Melling 2008).

To investigate the role of surface winds in modulating these transport pathways, we repeat the January Labrador Sea cable experiment for 20 iterations—this time adjusting all controls *except* atmospheric pressure to activate the controls influencing the target FW QoI (see e.g., Stewart and Haine 2013). The total cost is reduced by a factor of seven, with surface wind emerging as the dominant control, contributing approximately 45% of the total cost reduction. From the January mean adjustment made to JRA-55 winds (white arrows in Fig. 9a, enlarged in subplot Fig. 9b) we compute a wind stress curl adjustment featuring a dipole centered around Davis Strait: a positive

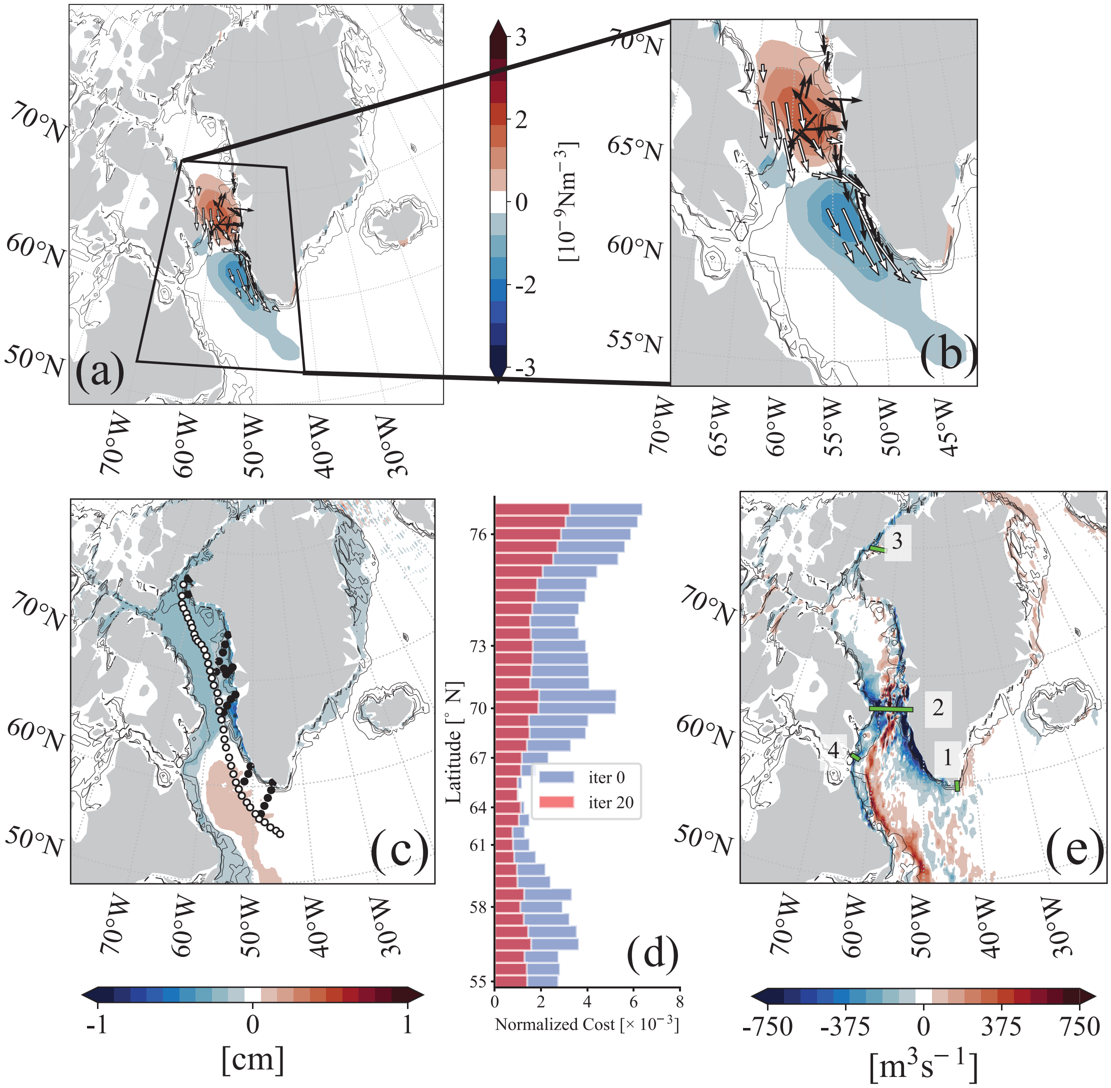

FIG. 9. (a) January mean wind (white arrows) and sea surface (black arrows) velocity adjustments, enlarged in (b). The surface currents exhibit Ekman transport, deflecting westward relative to the wind adjustments above. The resultant wind stress curl adjustment is shown in blue and red contours. (c) The January mean OBP adjusts in response, as coastally trapped barotropic waves on either side of the Labrador Sea perimeter move water off of the Labrador Sea shelf and into its center. The p_b misfit, i.e. sum of model-data p_b misfits at each sensor (dots) is reduced. (d) A histogram illustrates the p_b misfit reduction across the cable's central vein's sensors (filled white in (c)). Consequently, the advective FW flux adjusts (meridional component in (e)). Green ticks mark flux gateways across which the $\mathrm{ADV_{fw}}$ skill is assessed (Table 2). Black contours show geostrophic f/H isolines.

curl (red) over Baffin Bay and a negative curl (blue) over the Labrador Sea. The wind adjustment induces Ekman transport, affecting surface currents (black arrows in Fig. 9b, which have been enlarged for visibility). In Davis Strait, the local positive wind stress curl drives cyclonic flow and surface divergence, leading to a local decrease in sea surface height and in turn OBP. This can be seen in the mean OBP adjustment shown in filled contours in Fig. 9c, which has been computed following Equation 4. Recall from the discussion in Section 2d that while assimilation brings the FM OBP variability closer to that of the NR, the control adjustments needed to reduce J_{misfit} bring about a baseline shift in mean OBP. Therefore, mean OBP adjustment concisely captures the dynamical response from the surface forcing adjustments. The northward WGCC decreases in the face of southward surface current adjustment. Ekman transport deflects these coastal current adjustments west, which shifts water mass away from the coast and into the Labrador Sea. The negative coastal OBP adjustment is associated with the propagation of a coastally trapped barotropic wave along the WGCC. The same can be seen in the LSC adjustment. This mechanism is demonstrated in detail through SPNA and Arctic surface wind perturbation experiments in Fukumori et al. (2015). Barotropic waves roughly follow geostrophic f/H contours shown in black, where f is the Coriolis force and H is ocean depth (Chen et al. 2023). This OSSE's SMART sensors are shown as black points. In Fig. 9d, a histogram shows the SMART cable's sensors (along the cable's central vein, sensors filled white in Fig. 9c) all saw p_b misfit reduction after 20 iterations.

The coastally trapped wave adjustments impact the FM representation of meridional advective FW flux variability, $\mathrm{ADV}_{\mathrm{fw}}$, as seen in Fig. 9e. FW flux is computed with reference salinity 34.8 psu and is positive northwards. The decreased southward EGC rounds Cape Farewell (gate #1, Fig. 9e) and bifurcates; one branch leads to a weakened northward WGCC FW transport, while the other turns south in the Labrador Sea (decreased WGC, red streak). Note that this positive $\mathrm{ADV}_{\mathrm{fw}}$ adjustment represents a decrease in southwards flow. The coastally trapped WGCC wave adjustment continues to decrease FW transport through Davis Strait (gate #2). Concurrently, southward FW export from the Arctic through Nares Strait (gate #3) intensifies and meanders south along the western Baffin Bay coast. The strong southward (blue signal) FW export continues southward through Davis Strait to the Labrador Shelf (gate #4). Given the Labrador Current FW flux increased while the mass in that region decreased, we can infer that saline water was exported into the Labrador Sea. The improved $\mathrm{ADV}_{\mathrm{fw}}$ verified against the NR with skill computed across the four flux gates (Table 2). Across each gateway, $\mathrm{ADV}_{\mathrm{fw}}$ anomaly error was reduced. For clarity, skill in anomalies can equivalently be understood as an increased in explained variance (see Appendix A1): Assimilating p_b from the Labrador Sea cable increases the extent to which FM $\mathrm{ADV_{fw}}$ anomaly explains variability in NR $\mathrm{ADV_{fw}}$ anomaly.

	Gateway	$\mathrm{ADV_{fw}}$ skill %
1	Cape Farewell	0.05
2	Davis Strait	7.57
3	Nares Strait	5.00
4	West Labrador Sea	4.10

TABLE 2. Skill of the meridional component of advective FW transport ($\mathrm{ADV_{fw}}$) anomaly for gateways shown in Fig. 9e.

The results presented in this case study highlight the ability of SMART monitoring to better constrain large-scale FW pathways. Reducing uncertainty in the $\mathrm{ADV_{fw}}$ variability through the aforementioned gateways is especially valuable given the high uncertainty in Arctic FW transport—observations are scarce, and its redistribution is poorly constrained and rapidly evolving due to changing river runoff (Weiss-Gibbons et al. 2024), increased Greenland Ice Sheet melt (King et al. 2020), and shifts in regional export patterns (Zhang et al. 2021; Zhang and Du 2025). We have shown *in-situ* OBP acquisitions from a potential SPNA SMART cable may constrain regional atmospheric forcing (p_{atm} and wind) and, as a result, regional barotropic circulation and FW redistribution. A final key consideration is whether SMART provides a novel contribution to GOOS. To address this, we focus on assessing whether high frequency *in-situ* p_b observations from SMART complement monthly observations of large-scale OBP from satellites (GRACE).

e. GRACE-equivalent OSSE

The OSSE framework in this study provides a straightforward path to demonstrate how SMART's sub-monthly p_b observations can complement GRACE. Beginning from the NR's daily p_b data processed as described in Section 2, two additional steps were performed to generate "GRACE-equivalent" data. First, monthly mean p_b were computed from the daily records. The spatial scale of the data, having been binned from $1/48°$ to $1/3°$ resolution, are further binned, this time into blocks of side length roughly 300 km (or $\sim 3°$) reflecting the width of GRACE's mass concentration blocks or "mascons." A map of GRACE mascons was obtained from GRACE data from January 2012 mapped onto the ECCO $1/3°$ global grid (Zhang et al. 2018). The data was converted to an index map used to designate groups of neighboring grids for bin-averaging, resulting in a January-mean 2012 NR p_b field with a spatial resolution akin to GRACE. For consistency, we reconstruct the p_b representation uncertainty operator $\mathbf{\Gamma}_{\text{obs}}$ by modifying the procedure in Section 2d increasing the spatial bin-average size from 16×16 to 48×48 and computing the standard deviation over monthly rather than daily averaged NR records. While the spatial binning is necessary for faithful representation of GRACE-equivalent data, our findings below chiefly concern the resolution of temporal NR variabilty. We assimilate the NR's GRACE-equivalent January 2012 p_b into the FM and after one iteration compare the p_b adjustment to the one seen in the SPNA cable OSSE in Section 3a. Specifically, we compare the skill of assimilating January 2012 SMART cable p_b data (Fig. 10a; same as Fig. 5c with the saturation increased) with that from assimilating GRACE data (Fig. 10b). The positive p_b skill throughout the SPNA of the SMART cable assimilation compared to GRACE is striking. In both experiments, the RMSEs underlying these skills were computed across daily model diagnostics. The much smaller skill pattern in panel (b) compared to (a) almost everywhere and even negative in the Labrador Sea and Nordic Seas, indicates that assimilating monthly-mean GRACE-equivalent p_b does not improve the FM's representation of daily p_b. Similarly, the SMART cable OSSE yields an 8% skill in Davis Strait transport anomaly, far better than the analogous GRACE-equivalent experiment's -0.2% skill. This confirms the benefit of SMART cables' daily monitoring in explaining variability in sub-monthly NR quantities.

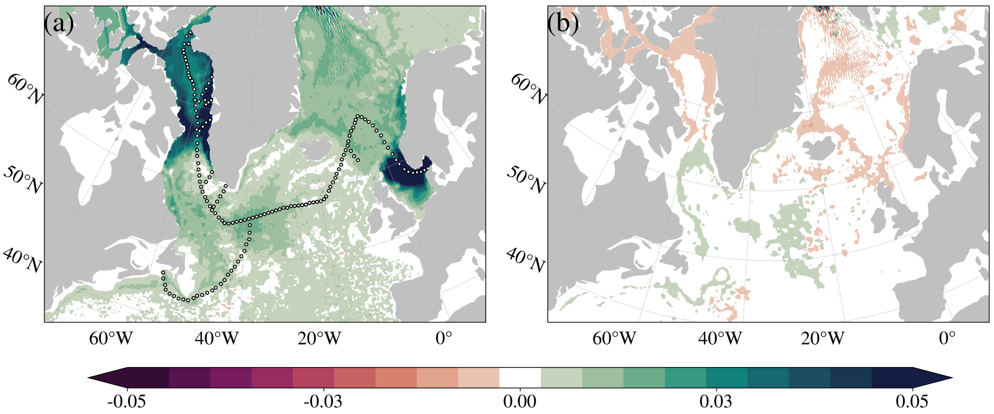

FIG. 10. Comparison between January 2012 p_b skill attained by assimilating (a) SMART cable and (b) GRACE-equivalent data from the NR. FM constraint to GRACE's monthly frequency is unable to improve representation of sub-monthly p_b, as evidenced by low and negative skill regions not observed in the largely positive SMART cable OSSE.

4. Conclusion

This study evaluated the potential of the SMART subsea cable observing system to constrain ocean bottom pressure in a regional general circulation model of the subpolar North Atlantic. SMART has emerged over the last decade as a proposed global initiative to leverage commercial subsea telecommunications cables for real-time geophysical observations, including ocean bottom pressure, temperature, and seismic activity. *In-situ* ocean bottom pressure measurements remain sparse yet critically important for understanding ocean mass redistribution and large-scale circulation. The proposed SMART cable route across the SPNA presents a unique opportunity to fill a major observational gap in a climatically sensitive region. The motivation for our observing system simulation experiments stems from the need to quantify how SMART data could enhance ocean state estimation prior to actual deployment.

To our knowledge, this work constitutes the first rigorous OSSE-based investigation into the impact of SMART observations on the ocean observing system. Previously, a study demonstrated OBP error reduction assimilating synthetic SMART observations obtained from the Max Planck Institute Ocean Model (unpublished manuscript by Tobias Weber, obtained through private communication). In contrast to their ensemble Kalman filter data assimilation approach, we use the dynamically and kinematically consistent adjoint method, which enables a thorough investigation into the physical mechanism underlying model p_b adjustment.

We found that improvements to representation of p_b variability were widespread, but strongest local to the cable path. The optimization was largely governed by adjustments to surface atmospheric pressure, consistent with prior studies, suggesting p_b variability on daily-to-weekly timescales to be strongly driven by p_{atm}. We also demonstrated that daily control adjustment is essential for fully capturing the benefit of daily SMART observations. When assimilation was conducted using a biweekly adjustment of the surface forcing control variables, which is the current standard in ECCO state estimates, p_b skill was low and, in some cases, even degraded due to likely temporal aliasing effects. This outcome underscores the importance of using more frequent control updates to fully realize the benefits of observations that are collected on a daily basis, such as those expected from a SMART system.

SMART's constraint on p_b was also found to increase explained variance in barotropic velocities and advective freshwater transports, highlighting that SMART's contribution to the global ocean observing system will impact more than the actual variables SMART senses directly. Dynamical teleconnections captured through adjoint-based sensitivity fields helped quantify the extent to which ocean dynamics exposed by the adjoint model mediates between local SMART pressure observations and remote oceanic properties. Moreover, the GRACE-equivalent OSSE highlighted the added benefit which SMART provides in constraining sub-monthly and coastal oceanic mass transport.

While our results are encouraging, the OSSEs were limited to short-window assimilation experiments of one month. This short duration is a limitation, given that many goals of ocean state estimation, such as monitoring large-scale phenomena evolving on seasonal to multi-decadal time scales, require analysis over much longer periods. Therefore, future SMART OSSEs should assess the potential impact of SMART observations over longer timescales. It is also important that future studies incorporate more realistic modeling of sensor performance, particularly the issue of bottom pressure sensor drift. Including synthetic drift models, such as the linear-plus-exponential formulation introduced by Hughes et al. (2012), would offer a more accurate representation of long-term sensor behavior.

The design of the SPNA SMART network is still evolving. While cable routing and sensor types will not be guided by science requirements, questions remain about optimal sensor spacing, placement on continental shelves versus flat bathymetry, and the number of observation points needed to maximize impact. OSSEs could play a pivotal role in addressing these design questions. For instance, the extent to which local p_b skill features can be refined will depend on the misfit's spatial smoothing radius, which dictates the spread of local control adjustments necessary for optimization. Other approaches such as Hessian uncertainty quantification (Loose and Heimbach 2021) offer pathways to quantify the complementarity of SMART observations with existing satellite (e.g., GRACE) and in-situ networks. This is a critical future step, as SMART may fill a unique niche in the high-latitude observing system, especially by providing continuous, high-frequency, and vertically integrated mass measurements unavailable from other devices.

Our study establishes a methodological foundation for evaluating the unique contribution of SMART cables to the global ocean observing system. Results shown encourage future assessment of both the potential constraint SPNA SMART offers on AMOC and the complementarity between SPNA SMART and existing SPNA in-situ observing networks (Section 1). Future efforts should build on this framework to explore inter-annual to multi-decadal impacts, integration with other observing systems, and observational complementarity in dynamically active regions such as the SPNA. In addition, SMART temperature sensors have the potential to provide sustained, high-resolution measurements of bottom boundary layer processes, which are important for examining turbulence and mixing and closing regional and global heat budgets. Future experiments should also investigate SMART acoustic sensing of sound speed along ray paths to obtain absolute water velocity along cables. These findings may further bolster SMART's position as a transformative component of the ocean observing system, offering novel insights on dynamics that are otherwise difficult to obtain.

APPENDIX A

A1. Relationship between RMSE and explained variance

Explained variance, defined

$$\mathrm{EV}(x,y) = 1 - \frac{\mathrm{Var}(x-y)}{\mathrm{Var}(x)} \tag{A1}$$

quantifies the extent to which one variable explains another (Fukumori et al. 2015). That is, EV is closer to 100% the more y accounts for variability in x. Consider one-dimensional zero-mean random variables x, y, and z (e.g. time-series of climate anomalies). Without loss of generality, the variance of such a variable is

$$\mathrm{Var}(x) = \mathbb{E}[x^2].$$

Next, with root-mean squared error defined $\mathrm{RMSE}(x,y) = \mathbb{E}[(x-y)^2]^{1/2}$, it follows that

$$\mathrm{RMSE}(x,y) = (\mathrm{Var}(x-y))^{1/2}.$$

Substituting into Equation (A1), we write the explained variance for mean-zero variables as

$$\mathrm{EV}(x,y) = 1 - \frac{\mathrm{RMSE}(x,y)^2}{\mathrm{Var}(x)}. \tag{A2}$$

The denominator $\text{Var}(x)$ is fixed and nonnegative, so clearly a decrease in $\text{RMSE}(x,y)$ increases $\text{EV}(x,y)$. Recalling the definition of skill introduced in Equation 5, we have

$$S = 1 - \frac{\text{RMSE}(x,y)}{\text{RMSE}(x,z)} = 1 - \frac{(\text{Var}(x-y))^{1/2}}{(\text{Var}(x-z))^{1/2}}.$$

Therefore, in the event that the set $\{x,y,z\}$ attains positive skill, $S > 0$ implies

$$\begin{gathered}(\text{Var}(x-y))^{1/2} < (\text{Var}(x-z))^{1/2} \\ \text{Var}(x)\,[1-\text{EV}(x,y)] < \text{Var}(x)\,[1-\text{EV}(x,z)] \\ \text{EV}(x,y) > \text{EV}(x,z)\end{gathered}$$

invoking Equation A1. In the context of an OSSE involving anomaly fields {x,y,z}=$\{\vartheta^{\text{NR}}, \tilde{\vartheta}, \vartheta\}$, this derivation provides an equivalent framework for understanding skill: a positive (negative) skill implies a relative increase (decrease) in the amount that ϑ explains ϑ^{NR} after data assimilation.

APPENDIX B

B1. Atmospheric pressure uncertainty

In Section 3b, atmospheric pressure uncertainty was derived from the standard deviation of JRA-55 data, but other formulations may be valid. Take for example Fig.B1a, which, like Fig. 6, shows a potential uncertainty field $\sigma_{p_{\text{atm}}}$ whose inverse square weights atmospheric pressure adjustments in an adjoint-based least squares data assimilation. Like the uncertainty fields used to weight control adjustments in ASTEr1, $\sigma_{p_{\text{atm}}}$ are constructed following Chaudhuri et al. (2014): the field is derived from the spread of p_{atm} values for the month of January 2012 across multiple atmospheric reanalysis products, namely JRA-55, the fifth generation ECMWF atmospheric reanalysis (ERA5, Dee et al. 2011), and the Japanese Reanalysis for Three Quarters of a Century (JRA-3Q, Kosaka et al. 2024). Fig. B1b shows the 90th percentile values of the magnitude of the atmospheric pressure adjustment seen after 20 iterations (i.e. the absolute value of Fig. 7d) normalized by $\sigma_{p_{\text{atm}}}$. The atmospheric pressure adjustment is within .1 standard deviations of the p_{atm} uncertainty, thus confirming reasonable adjustment magnitudes.

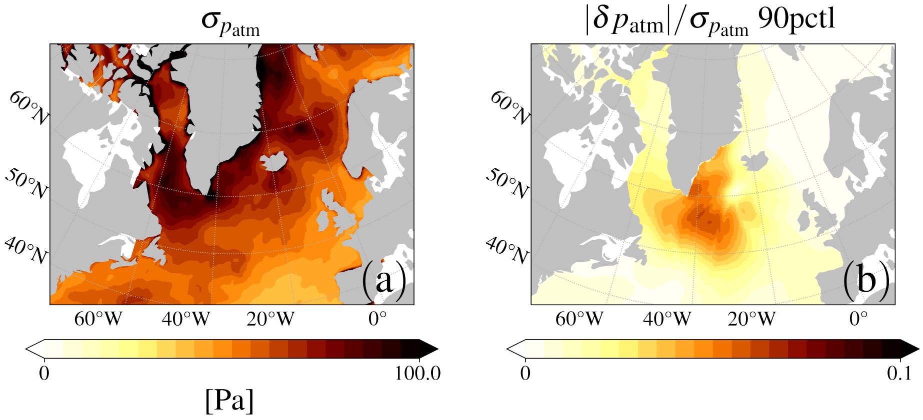

FIG. B1. (a) Atmospheric pressure uncertainty whose inverse square weights atmospheric pressure adjustments δp_{atm}. (b) The 90th percentile of p_{atm} adjustments scaled by $\sigma_{p_{\mathrm{atm}}}$ are small, indicating that the adjustments are, at least in magnitude, physical.

Using this p_{atm} uncertainty field, the Subpolar Gyre January OSSE is repeated, and the same mechanism in Fig. 7 is present once again (not shown): the negative-positive atmospheric pressure adjustment counterbalances and reduces the positive-negative spatial misfit dipole.

Acknowledgments.

This work was supported by the Gordon and Betty Moore Foundation through Grant GBMF10787. The adjoint model was generated using the AD tool Transformation of Algorithms in Fortran (TAF) by Fastopt.

Data availability statement.

The nature run data is accessible from ECCO's public data portal (`https://data.nas.nasa.gov/ecco/llc_4320/`). The forecast model is a configuration of ASTEr1, available at the Arctic Data Center (`https://arcticdata.io/catalog/portals/ASTE/ASTE`). The JRA-55 forcing dataset can be downloaded at (`https://climatedataguide.ucar.edu/climate-data/jra-55`). Modifications to the forecast model configuration, nature run extraction scripts, and data processing and analysis routines are available on GitHub (`https://github.com/mgoldberg10/smartosse`).

References

Adcroft, A., C. Hill, J.-M. Campin, J. Marshall, and P. Heimbach, 2004: Overview of the formulation and numerics of the MIT GCM. *Proceedings of the ECMWF Seminar on Recent Developments in Numerical Methods for Atmospheric and Ocean Modelling*, ECMWF, Reading, United Kingdom, 139–150.

Arbic, B. K., 2022: Incorporating tides and internal gravity waves within global ocean general circulation models: A review. *Prog. Oceanogr.*, **206**, 102 824, https://doi.org/10.1016/j.pocean.2022.102824.

Avsic, T., U. Send, and E. Skarsoulis, 2005: Six years of tomography observation in the central labrador sea. *International Conference Underwater Acoustic Measurements: Technologies and Results*, Heraklion, Greece, [Invited talk].

Bingham, R. J., and C. W. Hughes, 2008: The relationship between sea-level and bottom pressure variability in an eddy permitting ocean model. *Geophys. Res. Lett.*, **35**, L03 602, https://doi.org/10.1029/2007GL032662.

Campin, J.-M., A. Adcroft, C. Hill, and J. Marshall, 2004: Conservation of properties in a free-surface model. *Ocean Modelling*, **6**, 221–244, https://doi.org/10.1016/S1463-5003(03)00009-X.

Chaudhuri, A. H., R. M. Ponte, and A. T. Nguyen, 2014: A comparison of atmospheric reanalysis products for the arctic ocean and implications for uncertainties in air–sea fluxes. *J. Climate*, **27**, 5411–5421, https://doi.org/10.1175/JCLI-D-13-00424.1.

Chen, L., J. Yang, and L. Wu, 2023: Topography effects on the seasonal variability of ocean bottom pressure in the north pacific ocean. *J. Phys. Oceanogr.*, **53**, 929–941, https://doi.org/10.1175/JPO-D-22-0140.1.

Curry, B., C. M. Lee, B. Petrie, R. E. Moritz, and R. Kwok, 2014: Multiyear volume, liquid freshwater, and sea ice transports through davis strait, 2004–10. *J. Phys. Oceanogr.*, **44**, 1244–1266, https://doi.org/10.1175/JPO-D-13-0177.1.

Dee, D. P., S. M. Uppala, A. J. Simmons, P. Berrisford, P. Poli, S. Kobayashi, and et al., 2011: The era-interim reanalysis: Configuration and performance of the data assimilation system. *Quart. J. Royal Meteor. Soc.*, **137**, 553–597, https://doi.org/10.1002/qj.828.

Forget, G., J.-M. Campin, P. Heimbach, C. N. Hill, R. M. Ponte, and C. Wunsch, 2015: ECCO version 4: an integrated framework for non-linear inverse modeling and global ocean state estimation. *Geosci. Model Dev.*, **8**, 3071–3104, https://doi.org/10.5194/gmd-8-3071-2015.

Fujii, Y., and Coauthors, 2019: Observing system evaluation based on ocean data assimilation and prediction systems: On-going challenges and a future vision for designing and supporting ocean observational networks. *Front. Mar. Sci.*, **6**, https://doi.org/10.3389/fmars.2019.00417.

Fukumori, I., O. Wang, I. Fenty, G. Forget, P. Heimbach, and R. Ponte, 2017: Ecco central estimate (version 4 release 3). MITgcm-based ocean state estimate, https://ecco-group.org/products-ECCO-V4r3.htm.

Fukumori, I., O. Wang, W. Llovel, I. Fenty, and G. Forget, 2015: A near-uniform fluctuation of ocean bottom pressure and sea level across the deep ocean basins of the arctic ocean and the nordic seas. *Prog. Oceanogr.*, **134**, 152–172, https://doi.org/10.1016/j.pocean.2015.01.013.

Gallmeier, K., J. X. Prochaska, P. Cornillon, D. Menemenlis, and M. Kelm, 2013: An evaluation of the LLC4320 global-ocean simulation based on the submesoscale structure of modeled sea surface temperature fields. *Geosci. Model Dev.*, **16**, 7143–7170, https://doi.org/10.5194/gmd-16-7143-2023.

Giering, R., and T. Kaminski, 1998: Recipes for adjoint code construction. *ACM Trans. on Math. Software*, **24**, 437–474, https://doi.org/10.1145/293686.293695.

Haine, T. W., and Coauthors, 2015: Arctic freshwater export: Status, mechanisms, and prospects. *Global Planet. Change*, **125**, 13–35, https://doi.org/10.1016/j.gloplacha.2014.11.013.

Haine, T. W. N., 2020: Arctic ocean freshening linked to anthropogenic climate change: All hands on deck. *Geophys. Res. Lett.*, **47 (23)**, e2020GL090 678, https://doi.org/10.1029/2020GL090678.

Handmann, P., J. Fischer, M. Visbeck, J. Karstensen, A. Biastoch, C. Böning, and L. Patara, 2018: The deep western boundary current in the labrador sea from observations and a high-resolution model. *J. Geophys. Res. Oceans*, **123**, 2829–2850, https://doi.org/10.1002/2017JC013702.

Heimbach, P., C. I. Wunsch, R. M. Ponte, G. Forget, C. N. Hill, and J. Utke, 2011: Timescales and regions of the sensitivity of atlantic meridional volume and heat transport: Toward observing system design. *Deep-Sea Res. II: Top. Stud. Oceanogr.*, **58**, 1858–1879.

Hoffman, R., and R. Atlas, 2015: Future observing system simulation experiments. *Bull. Amer. Meteor. Soc.*, **97**, 1601—-1616, https://doi.org/10.1175/BAMS-D-15-00200.1.

Howe, B. M., and Coauthors, 2019: Smart cables for observing the global ocean: Science and implementation. *Front. Mar. Sci.*, **6**, https://doi.org/10.3389/fmars.2019.00424.

Hughes, C. W., M. E. Tamisiea, R. J. Bingham, and J. Williams, 2012: Weighing the ocean: Using a single mooring to measure changes in the mass of the ocean. *Geophys. Res. Lett.*, **39**, L17 602, https://doi.org/10.1029/2012GL052935.

Jahn, A., L. B. Tremblay, R. Newton, M. M. Holland, L. A. Mysak, and I. A. Dmitrenko, 2010: A tracer study of the arctic ocean's liquid freshwater export variability. *J. Geophys. Res. Oceans*, **115 (C7)**, https://doi.org/10.1029/2009JC005873.

Jones, D. C., G. Forget, B. Sinha, S. A. Josey, E. J. D. Boland, A. J. S. Meijers, and E. Shuckburgh, 2018: Local and remote influences on the heat content of the labrador sea: An adjoint sensitivity study. *J. Geophys. Res. Oceans*, **123**, 2646–2667, https://doi.org/10.1002/2018JC013774.

JTF Engineering Team, 2016: General requirements for sensor enabled reliable telecommunications (SMART) cable systems. White Paper Issue 1.0, Joint Task Force on SMART Cable Systems.

King, M., I. Howat, S. Candela, and Coauthors, 2020: Dynamic ice loss from the Greenland Ice Sheet driven by sustained glacier retreat. *Commun. Earth Environ.*, **1**, https://doi.org/10.1038/s43247-020-0001-2.

Kobayashi, S., and Coauthors, 2015: The JRA-55 reanalysis: General specifications and basic characteristics. *J. Meteor. Soc. Japan*, **93 (1)**, 5–48, https://doi.org/10.2151/jmsj.2015-001.

Kosaka, Y., and Coauthors, 2024: The JRA-3Q reanalysis. *J. Meteor. Soc. Japan*, **102**, 49–109, https://doi.org/10.2151/jmsj.2024-004.

Köhl, A., F. Siegismund, and D. Stammer, 2012: Impact of assimilating bottom pressure anomalies from grace on ocean circulation estimates. *J. Geophys. Res. Oceans*, **117**, C04 032, https://doi.org/https://doi.org/10.1029/2011JC007623.

Loose, N., and P. Heimbach, 2021: Leveraging uncertainty quantification to design ocean climate observing systems. *J. Adv. Model. Earth Sy.*, **13**, e2020MS002 386, https://doi.org/https://doi.org/10.1029/2020MS002386.

Loose, N., P. Heimbach, H. R. Pillar, and K. H. Nisancioglu, 2020: Quantifying dynamical proxy potential through shared adjustment physics in the north atlantic. *J. Geophys. Res. Oceans*, **125 (9)**, e2020JC016 112, https://doi.org/10.1029/2020JC016112.

Lozier, M. S., and Coauthors, 2017: Overturning in the subpolar north atlantic program: A new international ocean observing system. *Bull. Amer. Meteor. Soc.*, **98**, 737–752, https://doi.org/10.1175/BAMS-D-16-0057.1.

Marshall, J., A. Adcroft, C. Hill, L. Perelman, and C. Heisey, 1997: A finite-volume, incompressible Navier Stokes model for studies of the ocean on parallel computers. *J. Geophys. Res.*, **102**, 5753–5766, https://doi.org/10.1029/96JC02775.

Mercier, H., D. Desbruyères, P. Lherminier, A. Velo, L. Carracedo, M. Fontela, and F. F. Pérez, 2024: New insights into the eastern subpolar north atlantic meridional overturning circulation from OVIDE. *EGUsphere*, 1–27, https://doi.org/10.5194/egusphere-2024-388.

Münchow, A., and H. Melling, 2008: Ocean current observations from nares strait to the west of greenland: Interannual to tidal variability and forcing. *J. Mar. Res.*, **66**, 801–833, https://doi.org/10.1357/002224008788064612.

Na, H., D. R. Watts, J.-H. Park, C. Jeon, H. J. Lee, M. Nonaka, and A. D. Greene, 2016: Bottom pressure variability in the Kuroshio Extension driven by the atmosphere and ocean instabilities. **121**, 6507–6519, https://doi.org/10.1002/2016JC012097.

Nguyen, A. T., P. Heimbach, V. V. Garg, V. Ocaña, C. Lee, and L. Rainville, 2020: Impact of synthetic arctic argo-type floats in a coupled ocean–sea ice state estimation framework. *J. Atmos. Oceanic Technol.*, **37**, 1477–1495, https://doi.org/10.1175/JTECH-D-19-0159.1.

Nguyen, A. T., H. Pillar, V. Ocaña, A. Bigdeli, T. A. Smith, and P. Heimbach, 2021: The Arctic Subpolar Gyre sTate Estimate: Description and assessment of a data-constrained, dynamically consistent ocean-sea ice estimate for 2002–2017. *J. Adv. Model. Earth Sy.*, **13**, e2020MS002 398, https://doi.org/10.1029/2020MS002398.

Pacini, A., and R. S. Pickart, 2022: Meanders of the west greenland current near cape farewell. *Deep-Sea Res. I: Oceanogr. Res. Pap.*, **179**, https://doi.org/10.1016/j.dsr.2021.103664.

Pillar, H. R., P. Heimbach, H. L. Johnson, and D. P. Marshall, 2016: Dynamical attribution of recent variability in atlantic overturning. *J. Climate*, **29**, 3339–3352, https://doi.org/10.1175/JCLI-D-15-0727.1.

Rocha, C. B., S. T. Gille, T. K. Chereskin, and D. Menemenlis, 2016: Seasonality of submesoscale dynamics in the kuroshio extension. *Geophys. Res. Lett.*, **43**, 11,304–11,311, https://doi.org/10.1002/2016GL071349.

Stammer, D., and Coauthors, 2002: Global ocean circulation during 1992–1997, estimated from ocean observations and a general circulation model. *J. Geophys. Res. Oceans*, **107**, 1–27, https://doi.org/10.1029/2001JC000888.

Stepanov, V. N., and C. W. Hughes, 2006: Propagation of signals in basin-scale ocean bottom pressure from a barotropic model. *J. Geophys. Res. Oceans*, **111 (C12)**, 002, https://doi.org/https://doi.org/10.1029/2005JC003450.

Stewart, K. D., and T. W. N. Haine, 2013: Wind-driven arctic freshwater anomalies. *Geophys. Res. Lett.*, **40**, 6196–6201, https://doi.org/10.1002/2013GL058247.

Tapley, B. D., S. Bettadpur, M. Watkins, and C. Reigber, 2004: The gravity recovery and climate experiment: Mission overview and early results. *Geophys. Res. Lett.*, **31**, https://doi.org/10.1029/2004GL019920.

Tapley, B. D., and Coauthors, 2019: Contributions of GRACE to understanding climate change. *Nat. Clim. Change*, **5**, 358–369, https://doi.org/10.1038/s41558-019-0456-2.

Wang, J., L.-L. Fu, B. Qiu, D. Menemenlis, J. T. Farrar, Y. Chao, A. F. Thompson, and M. M. Flexas, 2018: An observing system simulation experiment for the calibration and validation of the surface water ocean topography sea surface height measurement using in situ platforms. *J. Atmos. Oceanic Technol.*, **35 (2)**, 281–297, https://doi.org/10.1175/JTECH-D-17-0076.1.

Wei, Y., and Coauthors, 2025: An assessment of spread in the ecco global ocean-sea ice state estimate due to atmospheric forcing uncertainty, manuscript submitted to J. Geophys. Res. Oceans.

Weiss-Gibbons, T., A. Tefs, X. Hu, T. Stadnyk, and P. G. Myers, 2024: Sensitivity of simulated arctic ocean salinity and strait transport to interannually variable hydrologic model based runoff. *J. Geophys. Res. Oceans*, e2023JC020536, https://doi.org/10.1029/2023JC020536.

Wunsch, C., and P. Heimbach, 2007: Practical global oceanic state estimation. *Phys. D: Nonlinear Phenom.*, **230**, 197–208, https://doi.org/10.1016/j.physd.2006.09.040.

Zeng, X., and Coauthors, 2020: Use of observing system simulation experiments in the United States. *Bull. Amer. Meteor. Soc.*, **101 (8)**, E1427–E1438, https://doi.org/10.1175/BAMS-D-19-0155.1.

Zhang, H., D. Menemenlis, and I. Fenty, 2018: ECCO LLC270 Ocean-Ice State Estimate. URL http://hdl.handle.net/1721.1/119821, ECCO Consortium. accessed 1 Aug 2025.

Zhang, J., and L. Du, 2025: Freshwater transport variation through Fram and Davis Strait influenced by atmospheric circulation. *Front. Mar. Sci.,*, **12**, https://doi.org/10.3389/fmars.2025.1608187.

Zhang, J., W. Weijer, M. Steele, and Coauthors, 2021: Labrador sea freshening linked to beaufort gyre freshwater release. *Nat. Commun.*, **12**, 1229, https://doi.org/10.1038/s41467-021-21470-3.